


RESEARCH

Open Access



Modeling cerebrospinal fluid dynamics across the entire intracranial space through integration of four-dimensional flow and intravoxel incoherent motion magnetic resonance imaging

Shigeki Yamada^{1,2*} , Tomohiro Otani³, Satoshi Ii^{4,5}, Hirotaka Ito⁶, Chifumi Iseki^{7,8}, Motoki Tanikawa¹, Yoshiyuki Watanabe⁹, Shigeo Wada³, Marie Oshima² and Mitsuhiro Mase¹

Abstract

Background Bidirectional reciprocal motion of cerebrospinal fluid (CSF) was quantified using four-dimensional (4D) flow magnetic resonance imaging (MRI) and intravoxel incoherent motion (IVIM) MRI. To estimate various CSF motions in the entire intracranial region, we attempted to integrate the flow parameters calculated using the two MRI sequences. To elucidate how CSF dynamics deteriorate in Hakim's disease, an age-dependent chronic hydrocephalus, flow parameters were estimated from the two MRI sequences to assess CSF motion in the entire intracranial region.

Methods This study included 127 healthy volunteers aged ≥ 20 years and 44 patients with Hakim's disease. On 4D flow MRI for measuring CSF motion, velocity encoding was set at 5 cm/s. For the IVIM MRI analysis, the diffusion-weighted sequence was set at six b-values (i.e., 0, 50, 100, 250, 500, and 1000 s/mm²), and the biexponential IVIM fitting method was adapted. The relationships between the fraction of incoherent perfusion (f) on IVIM MRI and 4D flow MRI parameters including velocity amplitude (VA), absolute maximum velocity, stroke volume, net flow volume, and reverse flow rate were comprehensively evaluated in seven locations in the ventricles and subarachnoid spaces. Furthermore, we developed a new parameter for fluid oscillation, the Fluid Oscillation Index (FOI), by integrating these two measurements. In addition, we investigated the relationship between the measurements and indices specific to Hakim's disease and the FOIs in the entire intracranial space.

Results The VA on 4D flow MRI was significantly associated with the mean f -values on IVIM MRI. Therefore, we estimated VA that could not be directly measured on 4D flow MRI from the mean f -values on IVIM MRI in the intracranial CSF space, using the following formula; $e^{0.2(f-85)} + 0.25$. To quantify fluid oscillation using one integrated parameter with weighting, FOI was calculated as $VA \times 10 + f \times 0.02$. In addition, the FOIs at the left foramen of Luschka had the strongest correlations with the Evans index (Pearson's correlation coefficient: 0.78). The other indices related with Hakim's disease were significantly associated with the FOIs at the cerebral aqueduct and bilateral foramina of Luschka. FOI at the cerebral aqueduct was also elevated in healthy controls aged ≥ 60 years.

*Correspondence:

Shigeki Yamada

shigekiyamada393@gmail.com

Full list of author information is available at the end of the article



© The Author(s) 2024. **Open Access** This article is licensed under a Creative Commons Attribution 4.0 International License, which permits use, sharing, adaptation, distribution and reproduction in any medium or format, as long as you give appropriate credit to the original author(s) and the source, provide a link to the Creative Commons licence, and indicate if changes were made. The images or other third party material in this article are included in the article's Creative Commons licence, unless indicated otherwise in a credit line to the material. If material is not included in the article's Creative Commons licence and your intended use is not permitted by statutory regulation or exceeds the permitted use, you will need to obtain permission directly from the copyright holder. To view a copy of this licence, visit <http://creativecommons.org/licenses/by/4.0/>. The Creative Commons Public Domain Dedication waiver (<http://creativecommons.org/publicdomain/zero/1.0/>) applies to the data made available in this article, unless otherwise stated in a credit line to the data.

Conclusions We estimated pulsatile CSF movements in the entire intracranial CSF space in healthy individuals and patients with Hakim's disease using FOI integrating VA from 4D flow MRI and f -values from IVIM MRI. FOI is useful for quantifying the CSF oscillation.

Keywords Cerebrospinal fluid dynamics, Idiopathic normal pressure hydrocephalus, Aging, Hakim's disease, Idiopathic normal pressure hydrocephalus, Aging, CSF motion, Fluid oscillation, 4D Flow MRI, Intravoxel incoherent motion, Diffusion-weighted image

Background

The dynamics of cerebrospinal fluid (CSF) have been demonstrated in many imaging studies and animal models, but remains mysterious. Complex CSF motions comprise a steady microflow produced by the rhythmic wavy movement of motile cilia on the ventricular wall surface [1, 2]; dynamic multidirectional pulsatile, laminar, and turbulent flows produced by pulsations of the brain and cerebral arteries [2–8], and an uncertain flow produced by respiration and head movement [9–12]. However, measuring very small complex CSF motions with a velocity of <0.1 cm/s had been difficult using conventional phase-contrast magnetic resonance imaging (MRI) [4, 13] and four-dimensional (4D) flow MRI [6, 7, 14–16]. Furthermore, previous CSF dynamic studies have measured pulsatile CSF motions in the ventricles, including the foramen of Magendie, cerebral aqueduct, and foramina of Monro, and subarachnoid spaces in the posterior fossa, including the prepontine cistern and craniocervical junction, but not in the Sylvian fissures or the convexity part of the subarachnoid spaces [3–8, 13–16]. Furthermore, these complex pulsatile CSF motions have been considered to be mainly driven by arterial pulsations [10, 15, 17, 18] and decrease with aging because of declines in brain volume, arterial elasticity, and circulating cerebral blood volume [6, 8, 19, 20]. These age-related changes in CSF dynamics and volumes, including metabolism, are of interest because they are thought to be associated with dementia and neurodegenerative diseases by impairing the excretion of neurotoxic wastes from the brain [18, 21–23]. Moreover, tightened sulci in high convexity [24–26] have been recognized as the most important imaging finding for Hakim's disease, which has been called idiopathic normal-pressure hydrocephalus [27] in contrast to brain atrophy in the elderly population. Accumulating evidence supports the hypothesis that various alterations in CSF dynamics contribute to disproportionately enlarged subarachnoid spaces and ventricles in Hakim's disease, which is considered an age-dependent chronic hydrocephalus. We previously reported the usefulness of the mean value of fraction of incoherent perfusion (f) on intravoxel incoherent motion (IVIM) MRI for evaluating small complex CSF motions in the entire intracranial CSF space, comparing brains with Hakim's disease with

healthy aging brains [28], although their direction and flow velocity could not be examined on IVIM MRI [29–31]. Le Bihan et al. described visualization of CSF motion in their first paper on IVIM MRI [29], and the possibility that f values could quantify CSF motion in their second paper [30]. Therefore, we hypothesized that complex CSF motions in the entire intracranial space could be simulated using flow velocity parameters on 4D flow MRI and f on IVIM MRI. Confirming this hypothesis may contribute to the elucidation of CSF dynamics in Hakim's disease and aging effects. Therefore, this study aimed to estimate CSF motion from dynamic pulsatile flow to fine microflow by integrating f on IVIM MRI and flow velocity parameters on 4D flow MRI. In addition, our second purpose is to elucidate how alterations in CSF dynamics contribute to enlarged subarachnoid spaces and ventricles in Hakim's disease, using high-resolution 3D morphological models of the ventricles and subarachnoid spaces in the entire intracranial space. Furthermore, this study compared the distribution of CSF motions in healthy aging volunteers with that in patients with Hakim's disease.

Methods

Study population

In total, 128 healthy volunteers aged ≥ 20 years who underwent both 4D flow MRI and IVIM MRI on a 3-T brain MRI scanner (Discovery MR 750W, GE Medical Systems, Inc. Chicago, IL, USA) from November 2020 to February 2022 were recruited from the medical staff, students, and their family members by open recruitment. The inclusion criteria for the volunteers were as follows: individuals who had no history of brain injury, brain tumor, or cerebrovascular disease on previous brain MRI and those who had never undergone brain MRI and had no neurological symptoms, including cognitive function. One volunteer aged 84 years was excluded from this study because he had a history of head surgery due to a head injury over 30 years ago. Patients' MRI data were used in an opt-out method, after their personal information was anonymized in a linkable manner. Furthermore, 25 patients diagnosed with Hakim's disease who underwent MRI using the same GE MRI machine as that in the volunteers until 2022 and 19 patients with Hakim's disease who underwent MRI using a Philips MRI machine

(Ingenia Elition 3.0 T Philips, Amsterdam, Netherlands) since 2023 were included in this study. All patients with Hakim's disease had radiological findings of disproportionately enlarged subarachnoid space hydrocephalus (DESH) [32–34], specifically ventricular dilatation, enlarged Sylvian fissure, and narrow sulci at high convexity [26], and triad symptoms of gait disturbance, cognitive impairment, and urinary incontinence, according to the third edition of the Japanese guidelines for the management of idiopathic normal-pressure hydrocephalus [35]. Of them, 26 patients (59%) underwent CSF removal (30–35 mL) via a lumbar tap and were evaluated for changes in their symptoms before and 1 and 2 days after the CSF tap test. Furthermore, 25 patients (57%) underwent CSF shunt surgery, and their symptoms improved by ≥ 1 point on the modified Rankin Scale and/or the Japanese grading scale [35]. Other patients were not recommended to undergo an aggressive tap test or shunt surgery because their symptoms were very mild or they could not walk, and no improvement in symptoms was observed after the tap test or shunt surgery.

Image acquisition

The sequence parameters for 4D flow MRI using a GE MRI machine were as follows: repetition time, variable (10–20 ms); echo time, variable (3–7 ms); flip angle, 8°; field of view, 200 mm; matrix size, 256 × 256; voxel size, 0.781 × 0.781 × 1.0 mm; number of cardiac phases, 12; and velocity encoding, 5 cm/s. The 4D flow sequence parameters for a Philips MRI machine were as follows: repetition time, variable (10–20 ms); echo time, variable (3–7 ms); flip angle, 8°; field of view, 200 mm; matrix size, 208 × 198; voxel size, 0.89 × 0.89 × 1.0 mm; number of cardiac phases, 8; and velocity encoding, 5 cm/s. The image range was in the mid-sagittal plane with a width of 30 mm (1.0 mm × 30 slices), encompassing areas from the bilateral foramina of Monroe to the upper cervical subarachnoid spaces. The imaging time was approximately 10 min, depending on the individual heart rate, which was synchronized with the peripheral pulse rate measured from the finger. Because the original T1-weighted magnitude images, including the 4D flow sequence set, did not have sufficient resolution, the 3D T2-weighted fast spin-echo sequence was alternatively performed to obtain additional anatomical information, with the following parameters: repetition time, 2000 ms; echo time, 85.3 ms; matrix 288 × 288; voxel size, 0.8 × 0.8 × 0.8 mm; and acquisition time, approximately 4 min.

For the IVIM analysis, diffusion-weighted imaging was performed in the axial plane using six b values (i.e., 0, 50, 100, 250, 500, and 1000 s/mm²). The sequence parameters of a GE MRI machine were as follows: repetition time, variable (6000–7000 ms); echo time, variable

(75–80 ms); flip angle, 90°; slice thickness, 3.0 mm; field of view, 220 mm; acquisition matrix size, 128 × 192; pixel size, 1.7 × 1.1 mm; acquisition time, approximately 2 min for total acquisition; motion-probing gradient, bipolar type. The IVIM sequence parameters for a Philips MRI machine were as follows: repetition time, variable (10–20 ms); echo time, variable (3–7 ms); flip angle, 90°; slice thickness, 3.0 mm; field of view, 220 mm; acquisition matrix size, 123 × 192; pixel size, 0.98 × 0.98 mm. The isotropic images were created from three orthogonal diffuse gradient pulse images.

4D flow MRI analysis

Details of the acquisition method for 4D flow MRI were described in our previous papers [6, 7, 20]. In summary, in the first step of 4D flow MRI, 3D velocity encoding data obtained from triaxial phase-contrast images of 4D flow MRI and morphological data of the intracranial CSF space obtained from 3D T2-weighted MRI were combined using a commercialized 4D flow application on an independent 3D volume analyzer workstation (SYNAPSE 3D; FUJIFILM Corporation, Tokyo, Japan), as shown in Fig. 1. In the second step, the area to be analyzed by 4D flow MRI was extracted. In the third step, automated polynomial fitting properly was used to correct for phase offsets, eddy currents and background noise, enabling accurate measurements of slow CSF flow velocities [36]. Finally, the 3D flow velocity vectors, including the average, maximum, and minimum values of triaxial velocities (cm/s), stroke volume ($\mu\text{L}/\text{heartbeat}$), net flow volume ($\mu\text{L}/\text{heartbeat}$), and reverse flow rate (%), were measured at nine regions of interest (ROIs) based on anatomical features: ventral and dorsal aspects of the foramen magnum, foramen of Magendie, lower and upper parts of the cerebral aqueduct, bilateral foramina of Monroe, premedullary cistern, and prepontine cistern on the orthogonal planes perpendicular to the mid-sagittal section and perpendicular to the main axis of CSF motion. Because the CSF moves bidirectionally, velocity amplitude (VA) (cm/s) was defined as the difference between the maximum velocity and the minimum velocity (typically the maximum velocity in the opposite direction) at each ROI.

Intravoxel incoherent motion analysis

IVIM analysis to quantitatively evaluate small pulsatile complex CSF motions was performed as previously reported [28]. In brief, from the six low b -values of DWI images (0, 50, 100, 250, 500, and 1000 s/mm²), the commercialized IVIM application on the SYNAPSE 3D workstation creates f maps, concurrently with other parameters, including apparent diffusion coefficient (ADC, mm²/s), true diffusion coefficient (D , mm²/s), and

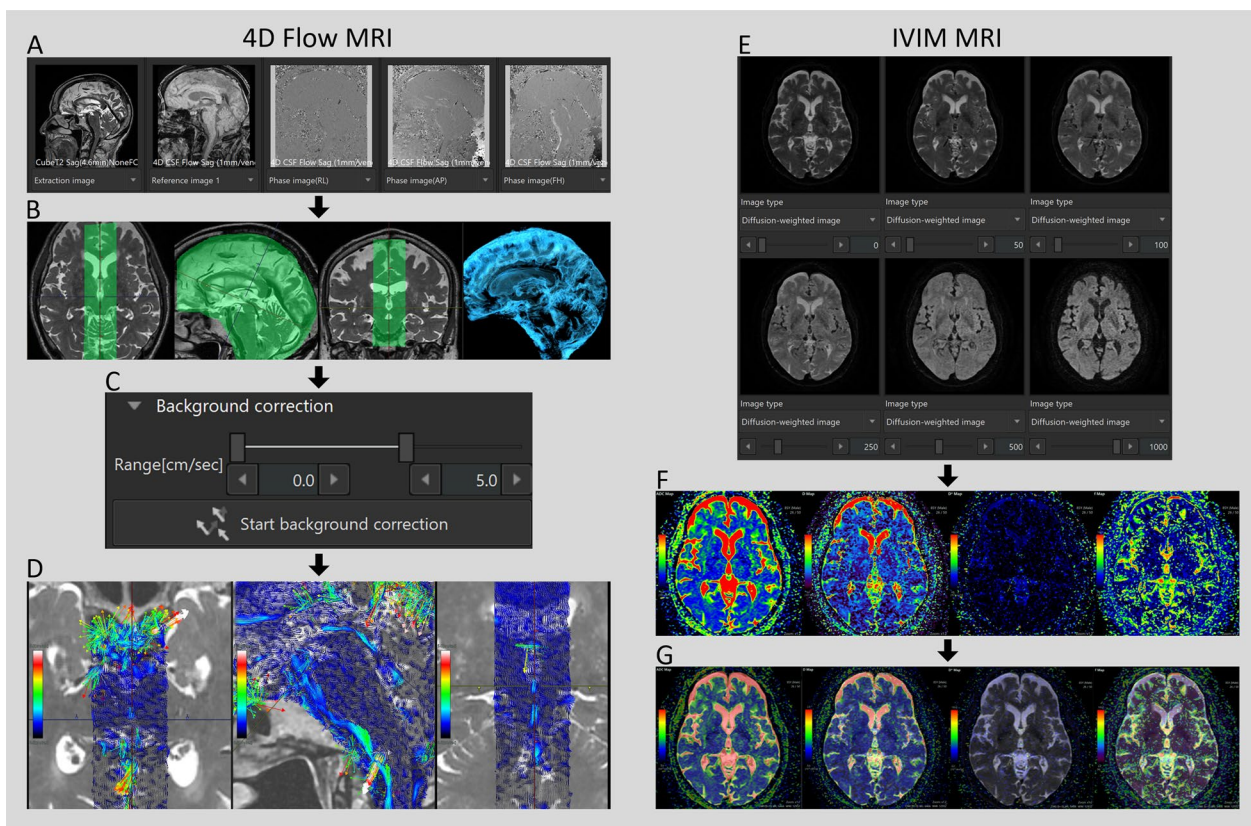


Fig. 1 Schema of our methods of 4D flow MRI and intravoxel incoherent motion (IVIM) MRI. The figures on the left illustrate (A–D) the 4D Flow MRI, while those on the right (E–G) depict the IVIM MRI, both acquired from a single healthy volunteer aged 85 years. **A** Demonstrates the initiation of the 4D Flow app. Four-dimensional analysis is performed utilizing the 3D T2-weighted MRI (leftmost), the morphological image of the 4D flow MRI (second from the left) as the reference, and tri-axis phase images (right three). Following the extraction of the area designated for 4D flow analysis (**B**, light green), background correction is executed (**C**), which is fully automated with a single click. Finally, an observation phase is undertaken to evaluate CSF flow velocity (**D**). In **E**, the IVIM app has just been launched, and all six low b-values of DWI images (0, 50, 100, 250, 500, and 1000 s/mm²) are integrated. The ADC map (leftmost), D map (second left), D* map (second right), and *f* map (rightmost) are automatically and instantly calculated (**F**). **G** Displays a b=0 DWI image automatically overlaid on four maps

pseudo-diffusion coefficient (*D*^{*}, mm²/s), in one voxel automatically and instantly (Fig. 1F).

We adapted the biexponential IVIM fitting method using the Levenberg–Marquardt algorithm with a constraint on *f* (0 < *f* < 1) as following equation:

$$\frac{S}{S_0} = f \cdot \exp(-bD^*) + (1 - f) \cdot \exp(-bD)$$

where *S* is the signal intensity at a given *b* value, *S*₀ is the signal intensity at *b*=0 s/mm². After IVIM analysis, *b*=0 DWI images were automatically superimposed on the *f* maps as shown in Fig. 1G. The average, maximum, and minimum values of *f* were measured in the following 45 ROIs based on anatomical features: the foramen magnum; bilateral foramina of Luschka; foramen of Magendie; fourth ventricle; lower and upper parts of the cerebral aqueduct; anterior and posterior parts of

the third ventricle; bilateral foramina of Monroe; anterior horn, body, trigone, and inferior horn of the bilateral lateral ventricles; bilateral cerebellopontine angle; prepontine cistern; interpeduncular cistern; lamina terminalis cistern; suprasellar or chiasmatic cistern; quadrigeminal cistern; bilateral ambient cisterns; bilateral carotid cisterns; anterior and posterior rami of the bilateral Sylvian sulci; bilateral Sylvian fossae; lower and upper parts of the interhemispheric fissure; bilateral superior frontal sulci; bilateral central sulci; and bilateral marginal sulci.

Fluid oscillation index

After comprehensive evaluation of the relationship between parameters on 4D flow MRI and *f*-values on IVIM MR, we developed a new parameter for fluid oscillation, the Fluid Oscillation Index (FOI), by integrating these two measurements.

Table 1 Clinical characteristics of the study population

| | Healthy volunteers | | | Hakim patients | P1 | P2 |
|--|--------------------|-------------|------------|----------------|--------|--------|
| | < 40 years | 40–59 years | ≥ 60 years | | | |
| Total number | 45 | 46 | 36 | 44 | | |
| Sex (female:male) | 30:15 | 32:14 | 21:15 | 28:16 | 0.071 | 0.550 |
| Age (years) | 29.2±5.4 | 49.4±5.8 | 69.2±6.9 | 77.1±7.0 | <0.001 | <0.001 |
| Evans index | 0.25±0.02 | 0.25±0.02 | 0.26±0.02 | 0.37±0.18 | <0.001 | 0.045 |
| Z-Evans index | 0.24±0.03 | 0.24±0.03 | 0.27±0.04 | 0.43±0.14 | <0.001 | <0.001 |
| BVR at AC | 2.1±0.3 | 2.1±0.3 | 1.8±0.4 | 0.83±0.27 | <0.001 | <0.001 |
| BVR at PC | 4.8±1.4 | 4.3±1.1 | 3.0±1.0 | 0.99±0.22 | <0.001 | <0.001 |
| Callosal angle (degree) | 119.9±9.4 | 118.7±11.4 | 117.0±11.5 | 68.9±16.7 | <0.001 | 0.614 |
| Area of the foramen of Magendie | 13.3±9 | 11.3±5.8 | 18.5±10.5 | 41.8±21.6 | <0.001 | 0.002 |
| Diameter of the foramen of Magendie | 3.1±1.4 | 2.8±1 | 3.5±1.2 | 6.7±2.5 | <0.001 | 0.104 |
| Diameter of the right foramen of Luschka | 1.4±0.8 | 1.7±0.9 | 1.7±1.0 | 3.4±1.5 | <0.001 | 0.290 |
| Diameter of the left foramen of Luschka | 1.7±0.9 | 2.3±1.2 | 2.2±1.2 | 3.7±1.4 | 0.002 | 0.014 |
| Total ventricles (mL) | 19.5±7.5 | 22±8.2 | 36.4±14.3 | 127±33.5 | <0.001 | <0.001 |
| Total ventricles (%) | 1.3±0.5 | 1.5±0.5 | 2.5±0.9 | 8.4±1.8 | <0.001 | <0.001 |
| Total subarachnoid spaces (mL) | 267±35.7 | 287±43.2 | 352±55.0 | 325±44.6 | 0.032 | <0.001 |
| Total subarachnoid spaces (%) | 18.2±2 | 20.1±2.3 | 24.5±2.7 | 21.6±2.5 | <0.001 | <0.001 |
| Total intracranial CSF space (mL) | 287±39.1 | 309±47.8 | 388±64.7 | 452±56.2 | <0.001 | <0.001 |
| Total intracranial CSF space (%) | 19.5±2.2 | 21.6±2.4 | 27.0±3.0 | 30.0±2.5 | <0.001 | <0.001 |

P1; probability value for the Mann–Whitney–Wilcoxon test between patients with Hakim's disease and healthy volunteers aged ≥ 60 years

P2; probability value for the Kruskal–Wallis test among the three age groups of healthy volunteers

Sex differences were compared using Fisher's exact test

AC anterior commissure, PC posterior commissure, CSF cerebrospinal fluid, BVR brain per ventricle ratio, AC anterior commissure, PC posterior commissure

Measurements and indices specific to Hakim's disease

The total ventricles and subarachnoid spaces were manually segmented from the 3D T2-weighted cube sequence using our original method combined with a simple threshold algorithm and manual segmentation, as previously reported [33, 34, 37]. Furthermore, the area and maximum anteroposterior diameter of the foramen of Magendie and the maximum anteroposterior diameter of the bilateral foramina of Luschka were measured. The indices specific to Hakim's disease—the Evans index defined as the maximal width of the frontal horns of the lateral ventricles to the maximal width of the internal diameter of the cranium based on the x-dimension; Z-Evans index defined as the maximum z-axial length of the frontal horns of the lateral ventricles to the maximum cranial z-axial length on the coronal plane, which was perpendicular to the anteroposterior commissure plane on the anterior commissure [33]; brain per ventricle ratios (BVRs) defined as the maximum width of the brain just above the lateral ventricles divided by the maximum width of the lateral ventricles on the reference coronal planes at the anterior commissure and posterior commissure levels, respectively [34]; and callosal angle defined as the angle of the roof of the bilateral ventricles on the

coronal plane at the posterior commissure level [38]—were measured.

Statistical analysis

The volunteers were divided into the following three subgroups according to their ages at the time of MRI examination: <40 years, 40–59 years, and ≥60 years. The mean ± standard deviation (SD) for several measurements and indices in the three age subgroups were compared using the Kruskal–Wallis rank sum test, and those in patients with Hakim's disease and healthy elderly aged ≥60 years were compared using the Mann–Whitney–Wilcoxon test. The chi-square test was used to compare the proportions of the groups. The relationship between the mean *f*-values on IVIM MRI and flow parameters measured on 4D flow MRI, such as VA, absolute maximum velocity, mean velocity, stroke volume, net flow volume, and reverse flow rate at the following seven ROIs: left and right foramina of Monroe, upper and lower parts of the cerebral aqueduct, foramen of Magendie, dorsal part of the foramen magnum, and prepontine cistern. These parameters were investigated using Pearson's correlation coefficient (*r*) and 95% confidential intervals (CIs). The ROI of the lower part of the cerebral aqueduct for 4D flow MRI was treated as the ROI of the upper part

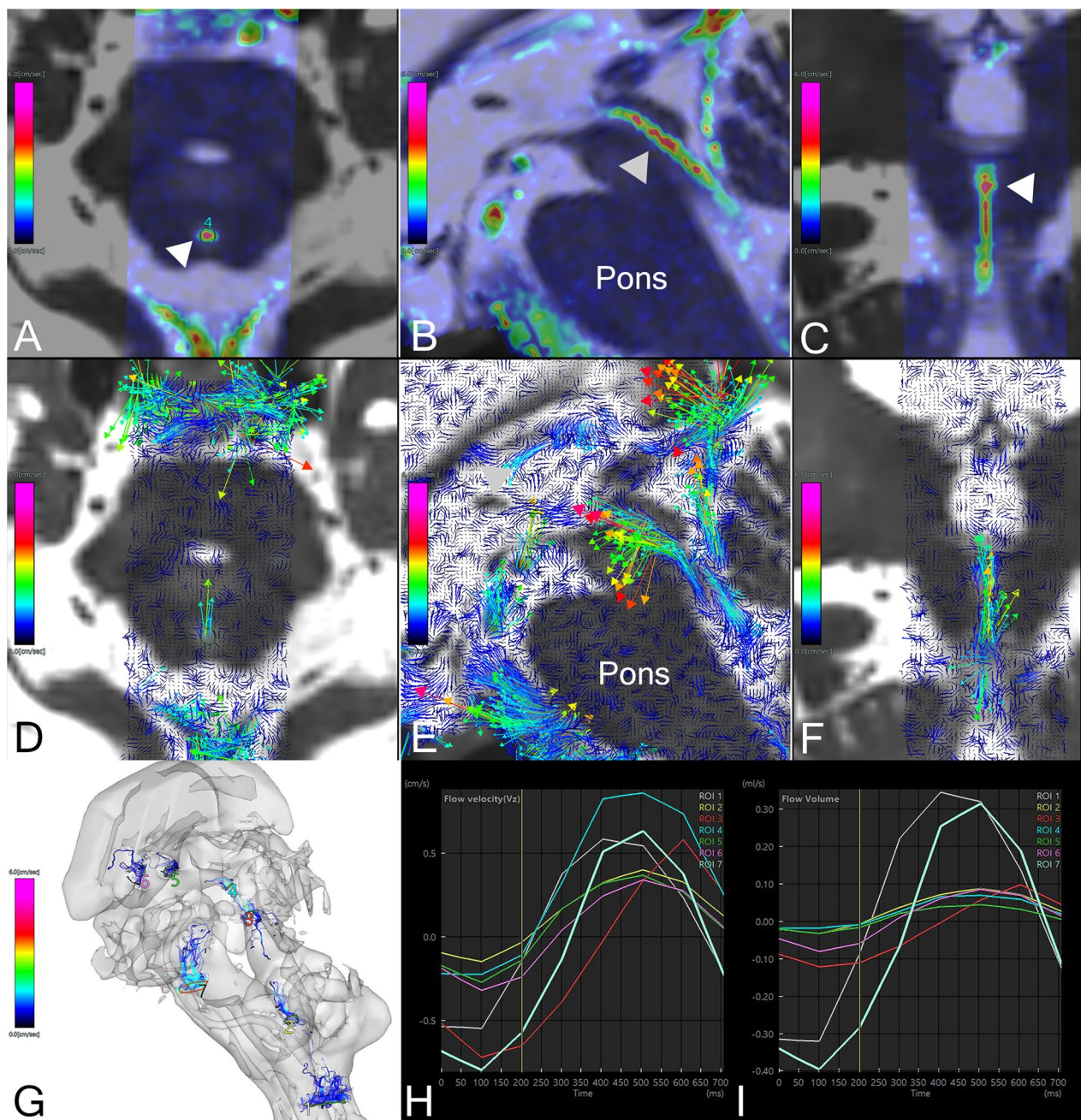


Fig. 2 Four-dimensional flow magnetic resonance imaging. The axial (A) sagittal (B) and coronal (C) colormap views of 4D flow MRI analysis show the velocity magnitude of CSF movements around the cerebral aqueduct (white arrowheads) in a representative patient with Hakim’s disease (73 years old, female). The colored area indicates the area where the 3D flow velocity (cm/s) was measured on 4D flow MRI, and the color bar indicates the magnitude of the 3D velocity of reciprocating CSF movements: red for fast and blue for slow. The 2D sagittal views of flow vectors (D–F) show the CSF movements with direction and velocity. The color and size of arrows indicate the velocity magnitude. The 3D view of streamlines (G) shows the CSF movements through seven ROIs during a heartbeat (a movie of the streamlines was attached to the supplemental materials). The line graph H shows the flow velocity and the line graph I shows the flow volume at seven ROIs. The ROIs were manually drawn at seven points, including the dorsal aspects of the foramen magnum (ROI1), foramen of Magendie (ROI2), lower (ROI3) and upper (ROI4) parts of the cerebral aqueduct, left (ROI5) and right (ROI6) foramina of Monro, and prepontine cistern (ROI7). The line graphs show the temporal changes of flow velocity (H) and flow volume (I) at these ROIs during the cardiac cycle

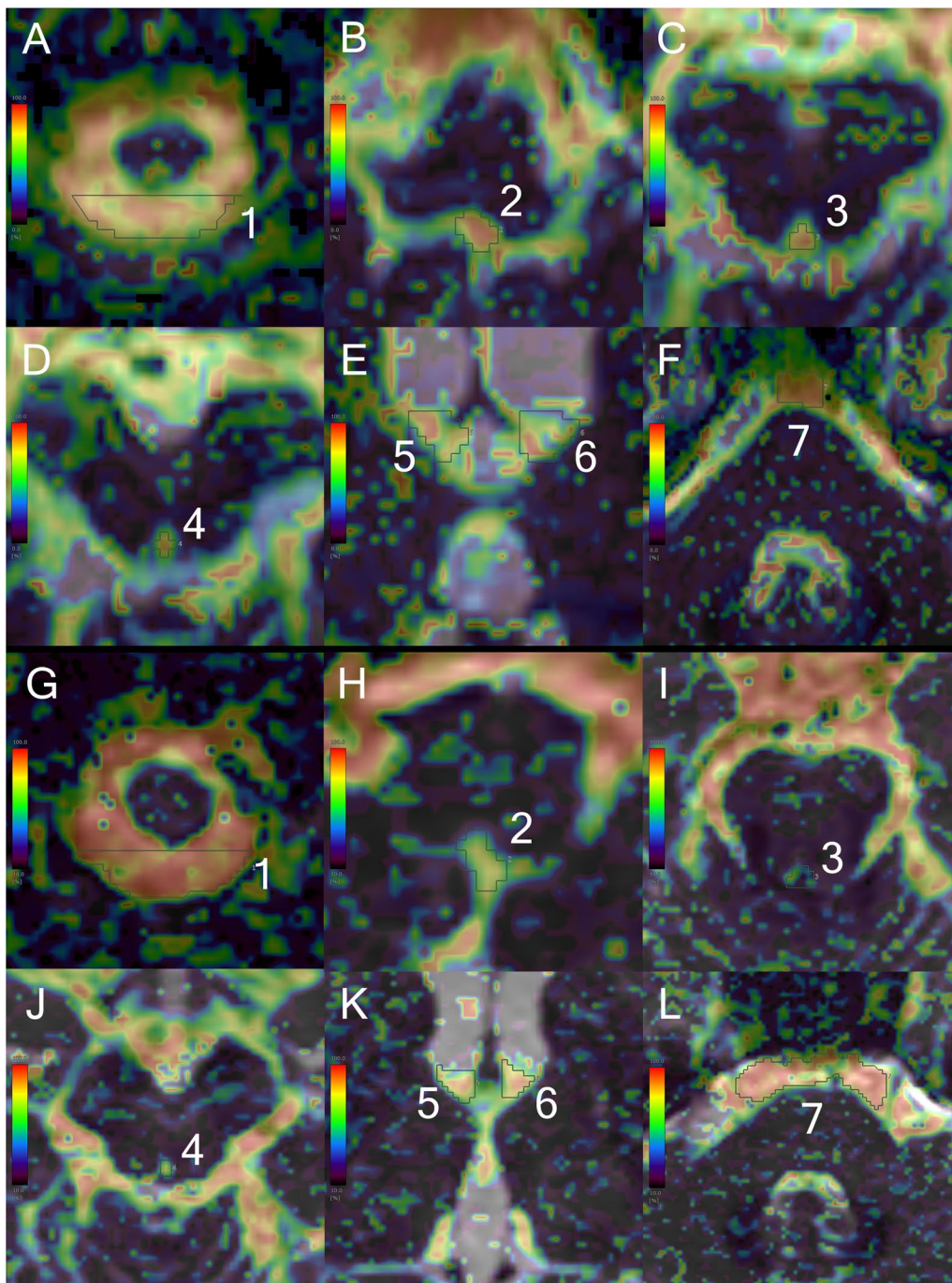


Fig. 3 Intravoxel incoherent motion f -map in a patient with Hakim's disease and healthy control. The upper **A–F** figures show the f -maps focused on seven ROIs in the same patient with Hakim's disease as Fig. 2, and the lower **G–L** figures show the f -maps in a representative healthy volunteer with the same age and sex as the patient with Hakim's disease (73 years old, female). The ROIs were manually drawn at seven points, including the dorsal aspects of the foramen magnum (ROI1) in **A** and **G**, foramen of Magendie (ROI2) in **B** and **H**, lower part of the cerebral aqueduct (ROI3) in **C** and **I**, upper part of the cerebral aqueduct (ROI4) in **D** and **J**, left (ROI5) and right (ROI6) foramina of Monro in **E** and **K**, and prepontine cistern (ROI7) in **F** and **L**. The color bar indicates the magnitude of the f -values on IVIM MRI: red for fast and blue for slow

Table 2 Stroke volume (μL/min) and velocity amplitude (VA) (cm/s) on 4D flow MRI and *f* (%) on IVIM MRI

| Region of interest | Stroke volume (μL/min) | VA (cm/s) | <i>f</i> (%) |
|--|------------------------|-------------|--------------|
| Foramen magnum, mean ± SD | 237 ± 145 | 1.33 ± 0.61 | 70.2 ± 16.6 |
| (Range) | (40–1100) | (0.20–4.85) | (9.2–94.6) |
| Prepontine cistern, mean ± SD | 162 ± 104 | 1.27 ± 0.72 | 87.3 ± 4.5 |
| (Range) | (20–600) | (0.27–6.37) | (65.9–95.4) |
| Foramen of Magendie, mean ± SD | 27.2 ± 23.3 | 0.49 ± 0.32 | 76.4 ± 8.4 |
| (Range) | (0–150) | (0.10–2.14) | (36.6–93.4) |
| Lower part of cerebral aqueduct, mean ± SD | 33.0 ± 29.6 | 0.78 ± 0.50 | 75.6 ± 7.5 |
| (Range) | (0–220) | (0.14–3.40) | (45.5–89.9) |
| Upper part of cerebral aqueduct, mean ± SD | 32.0 ± 35.2 | 0.94 ± 0.70 | 71.2 ± 11.1 |
| (Range) | (0–170) | (0.07–3.53) | (30.6–89.7) |
| Left foramen of Monroe, mean ± SD | 34.3 ± 34.0 | 0.48 ± 0.26 | 74.7 ± 12.9 |
| (Range) | (0–220) | (0.07–1.56) | (29.9–92.8) |
| Right foramen of Monroe, mean ± SD | 29.1 ± 24.7 | 0.41 ± 0.26 | 72.8 ± 14.2 |
| (Range) | (0–120) | (0.05–1.67) | (8.6–92.5) |

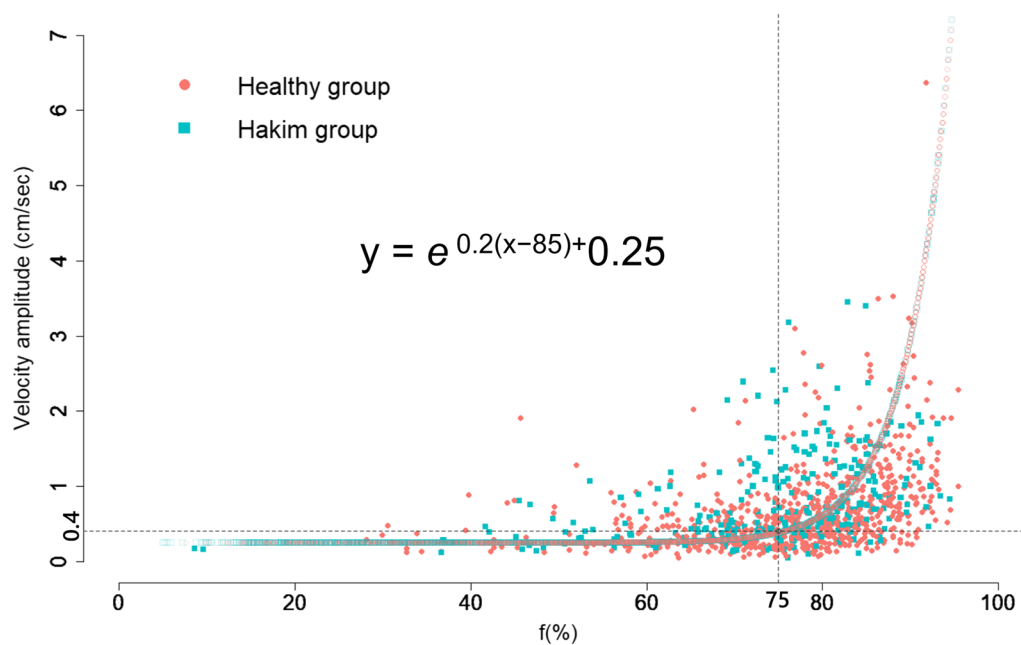


Fig. 4 Distribution of *f* on IVIM MRI and velocity amplitude (VA) on 4D flow MRI. The scatter plot shows the relationship between the *f* (%) on IVIM MRI (x axis) and VA (cm/s) on 4D flow MRI (y axis). The color plots and lines indicate the healthy group (salmon pink) and patients with Hakim’s disease (sky blue). Filled-in points represent actual measurements, while hollowed-out points represent estimates calculated using the following formula: $e^{0.2(x-85)+0.25}$. The dot vertical line indicates *f* = 75%, horizontal line VA = 0.4 cm/s

of the fourth ventricle for IVIM MRI. In addition, we investigated the relationship between the measurements and indices specific to Hakim’s disease and the FOIs in the entire intracranial space. Statistical significance was assumed at a probability (*P*) value of <0.05. All missing data points were treated as deficit data that did not affect other variables. Statistical analyses were performed using

R (version 4.2.3; The R Foundation for Statistical Computing; <http://www.R-project.org>).

Results

Clinical characteristics

In this study, 127 healthy volunteers (<40 years, n = 45; 40–59 years, n = 46; ≥ 60 years, n = 36), including 44 males

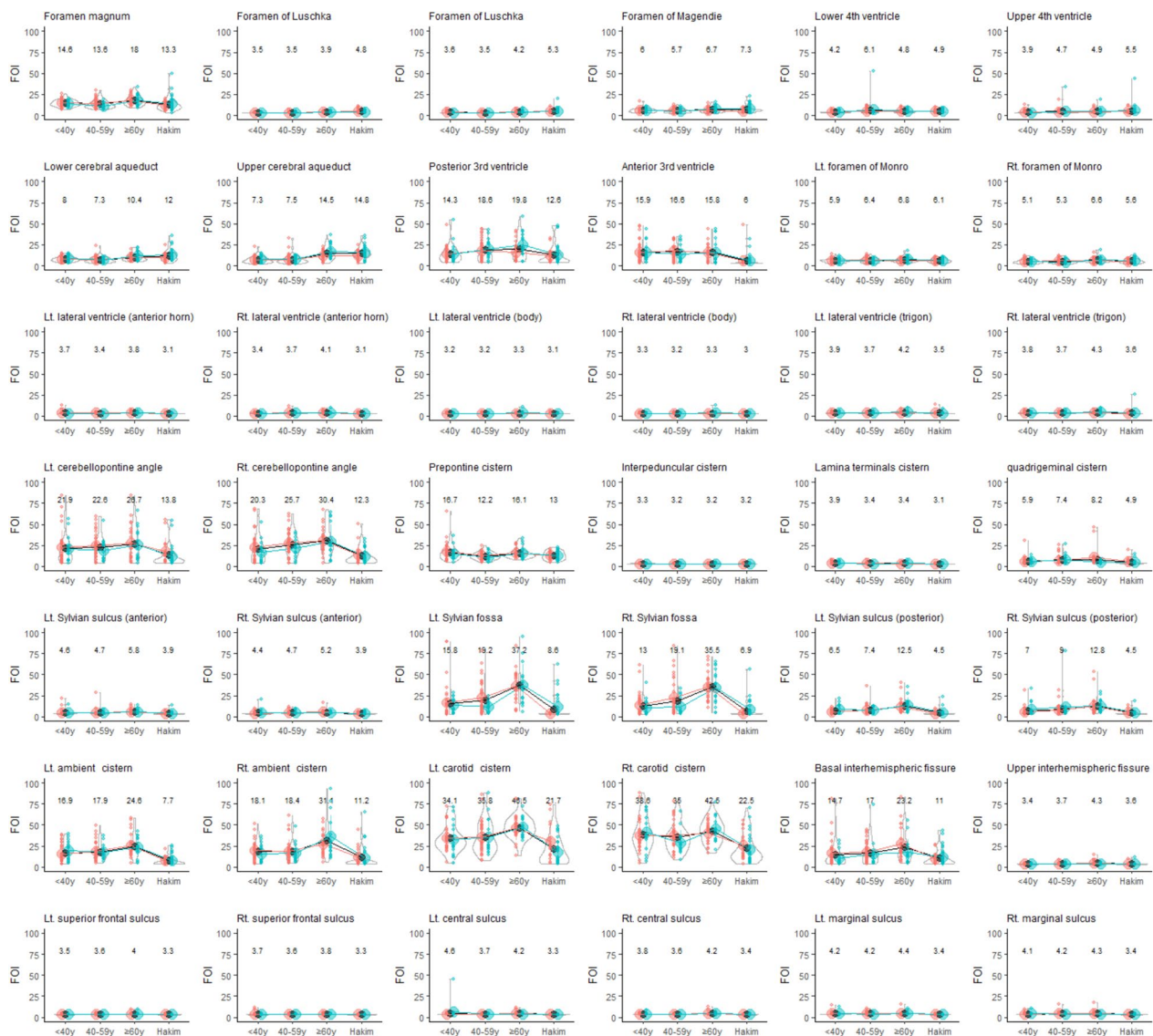


Fig. 5 Distribution of fluid oscillation index (FOI) among healthy controls and Hakim patients. Each graph is a combination of violin plots for the distribution of the VA and line graphs for the mean volume in each age group of healthy volunteers and Hakim group stratified according to sex. Salmon pink indicates female, sky blue indicates male, and black indicates all. The vertical lines contain the volumes between the 25th and 75th percentiles. The mean FOI in each group is shown above the violin plot

and 83 females, and 44 Hakim’s patients (77.1 ± 7.0 years), including 28 males and 16 females, were included. The linear and volumetric indices for the size of the intracranial CSF space, including the ventricular systems, among the three age groups of healthy volunteers and patients with Hakim’s disease are summarized in Table 1. Significant differences in all measurements were observed between patients with Hakim’s disease and healthy elderly individuals aged ≥ 60 years.

Relationship between flow parameters on 4D flow MRI and f-values on IVIM MRI

The flow parameters on 4D flow MRI at seven ROIs (Fig. 2 and supplemental movie) were comprehensively assessed to determine their relationship with the mean f-values on IVIM MRI at the same location (Fig. 3). Table 2 shows the averages and ranges of stroke volume and VA measured by 4D Flow MRI and f-values measured by IVIM MRI at 7 ROIs. Based on these averages and ranges of these parameters, we were unable to

determine which specific 4D flow MRI parameters correspond to the f -values optimally.

Estimation of CSF movement from the f -values on IVIM MRI and fluid oscillation index (FOI)

In order to elucidate the optimal 4D flow MRI parameters corresponding to f on IVIM MRI, a scatter plot was constructed to visualize the distribution of all f -values and VAs measured at 7 ROIs (Fig. 4).

Based on this distribution, it was deemed inappropriate to employ a linear regression model, and instead, fitting the data to a nonlinear exponential curve was considered to be the optimal approach. The exponential curve of $e^{0.2(x-85)} + 0.25$ was derived to best fit the distribution, providing a more accurate representation of the relationship between the f -values and VAs. From this regression equation, it was determined that VA corresponds to 0.4 cm/s when f is 75%. The utility of f surpassed that of VA in assessing flow oscillations when f -values were below 75%; conversely, VA proved more informative when f exceeded 75%. Consequently, in light of these findings, we introduced a novel index, FOI, calculated as VA (or estimated VA) $\times 10 + f \times 0.02$, which integrates these distinct parameters to quantitatively evaluate fluid oscillation. The distributions of FOIs across the entire intracranial space in the three age groups of healthy controls and the Hakim group are depicted in violin plots by sex (Fig. 5). FOIs were relatively large in the posterior subarachnoid space, foramen magnum, cerebral aqueduct, third ventricle, and Sylvian fossa, and very low in the lateral ventricles and the high parietal convexity part of the subarachnoid spaces.

Relationship between measurements and indices specific to Hakim's disease and fluid oscillation index (FOI)

We comprehensively examined the relationship between the morphological characteristics of Hakim's disease and FOIs at 45 ROIs using correlation matrices. As shown in

Fig. 6, the strongest correlations were observed between FOI at the left foramen of Luschka (ROI3) and the Evans index (r , 0.76; 95% CIs, 0.69 to 0.82; $p < 0.001$). The other indices related to Hakim's disease including ventricular volume ratio (%) were significantly associated with the FOIs at the cerebral aqueduct (ROI7 and 8) and the bilateral foramina of Luschka (ROI2 and 3), rather than the foramen of Magendie (ROI4). The ROIs showing significant correlations with ventricular volume ratio (%) in Fig. 6 are summarized in Table 3.

Discussion

In this study, we proposed a novel method for estimating CSF motion throughout the entire intracranial CSF space by integrating flow velocity data from 4D flow MRI and f from IVIM MRI (Fig. 7). Although 4D flow MRI can three-dimensionally measure the velocity and direction of CSF motions, the range of velocity measurement depends on velocity encoding. Conversely, IVIM MRI could not directly measure the velocity and direction of CSF motions; however, it could visualize and quantify very small CSF motions that could not be measured using 4D flow MRI. Furthermore, IVIM MRI can provide an overview of all CSF movements driven by arterial pulsations, brain pulsations produced by the cerebral blood circulation, respiration, and coordinated directional beating of the motile cilia, except for head movements, because it does not require heart-beat or respiration synchronization. Therefore, we investigated whether the flow information from the two MRI methods could be used to simulate the overall intracranial flow.

From the distribution of VA on 4D Flow MRI and f on IVIM MRI in Fig. 4, VA, reciprocating bidirectional CSF motion or oscillation, should be evaluated with a focus on VA rather than f , when the VA exceeds 0.4 cm/s. Conversely, when the VA is below 0.4 cm/s, f rather than VA would be better suited for evaluating reciprocating CSF

(See figure on next page.)

Fig. 6 Correlation matrix between morphological parameters for Hakim's disease and fluid oscillation index (FOI) in the entire intracranial CSF space. The correlation matrix is a comprehensive correlation analysis between parameters that indicate the morphological characteristics of Hakim's disease and FOI. As shown in the color bar on the right, the red gradient indicates the strength of the positive correlation, whereas the blue gradient indicates the strength of the negative correlation. Furthermore, the numbers written inside were Pearson's correlation coefficients. F foramen, SAS subarachnoid space, CSF cerebrospinal fluid. The numbers of regions of interests (ROIs) indicate the following regions: the foramen magnum (ROI1), right and left foramina of Luschka (ROI2 and 3), foramen of Magendie (ROI4), lower part of 4th ventricle (ROI5), 4th ventricle (ROI6), lower part of cerebral aqueduct (ROI7), upper part of cerebral aqueduct (ROI8), anterior part of 3rd ventricle (ROI9), posterior part of cerebral aqueduct (ROI10), right and left foramina of Monro (ROI11 and 12), right and left lateral ventricles (anterior horn ROI13 and 14, body ROI15 and 16, trigone ROI17 and 18, and inferior horn ROI19 and 20), right and left cerebellopontine angle (ROI21 and 22), prepontine cistern (ROI23), interpeduncular cistern (ROI24), lamina terminalis cistern (ROI25), suprasellar or chiasmatic cistern (ROI26), quadrigeminal cistern (ROI27), right and left ambient cisterns (ROI28 and 29), right and left carotid cisterns (ROI30 and 31), right and left Sylvian sulci (anterior ROI32 and 33, and posterior ROI36 and 37), right and left Sylvian fossae (ROI34 and 35), basal interhemispheric fissure (ROI38), upper part of interhemispheric fissure (ROI39), right and left superior frontal sulci (ROI40 and 41), right and left central sulci (ROI42 and 43), and right and left marginal sulci (ROI44 and 45)

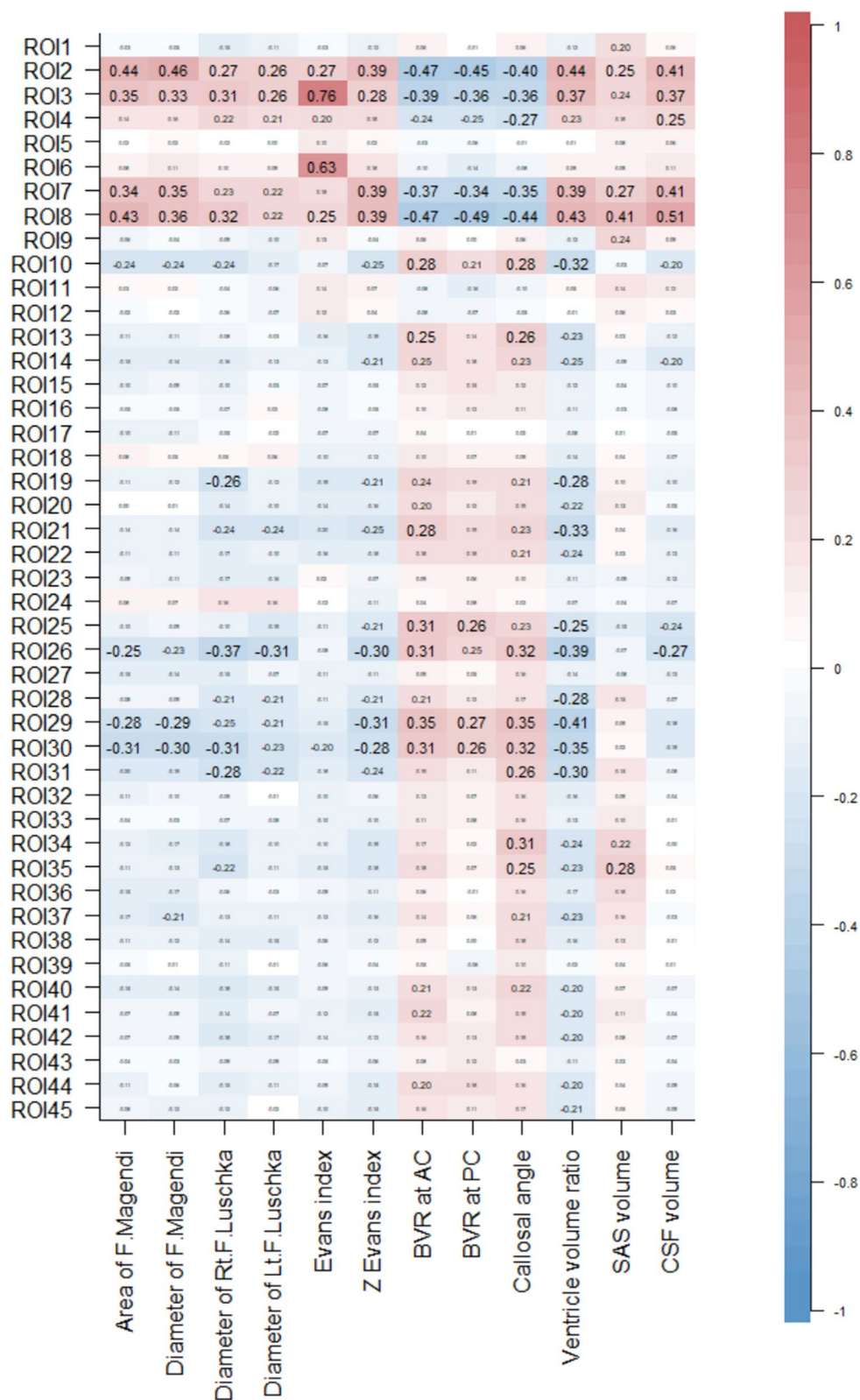


Fig. 6 (See legend on previous page.)

Table 3 Pearson’s correlation coefficient (*r*) and 95% confidential intervals (95% CIs) for the relationship between ventricular volume ratio (%) and fluid oscillation index (FOI)

| ROI number | ROI name | <i>r</i> (95% CIs) |
|------------|--------------------------------|------------------------|
| ROI2 | Rt. foramen of Luschka | 0.44 (0.32–0.56) |
| ROI3 | Lt. foramen of Luschka | 0.37 (0.24–0.50) |
| ROI7 | Lower end of cerebral aqueduct | 0.39 (0.26–0.51) |
| ROI8 | Upper end of cerebral aqueduct | 0.43 (0.30–0.54) |
| ROI10 | 3rd ventricle (anterior part) | −0.32 (−0.45 to −0.18) |
| ROI21 | Rt. cerebellopontine angle | −0.33 (−0.46 to −0.19) |
| ROI26 | Suprasellar cistern | −0.39 (−0.51 to −0.26) |
| ROI29 | Lt. ambient cistern | −0.41 (−0.53 to −0.28) |
| ROI30 | Rt. carotid cistern | −0.35 (−0.47 to −0.21) |
| ROI31 | Lt. carotid cistern | −0.30 (−0.43 to −0.15) |

motion. Based on the relationship between VA and *f*, a new FOI was created to comprehensively evaluate CSF oscillations by integrating both variables.

The major driving force of CSF movements is the pulsation of the brain due to cerebral circulation [2, 8, 20, 28, 39]. Brain pulsation generates and propagates waves in the CSF, and pressure gradients cause the CSF to move. Age-related changes in the intracranial environment require consideration of not only a decrease in brain volume [40, 41] but also an increase in CSF in the ventricles and subarachnoid space, a decrease in the total cerebral

blood flow volume due to a decrease in brain volume [42], and a further decrease in pulsatile CSF movements due to a decrease in the cerebral blood flow volume. Compared with healthy aging volunteers, patients with Hakim’s disease had a significantly larger intracranial CSF volume, which is distributed disproportionately, such as ventricular dilatation, enlarged Sylvian fissure, and narrow sulci at high parietal convexity; these are collectively called DESH [32–34]. The reasons for the development of DESH, particularly the narrow sulci at high parietal convexity, remain to be fully elucidated. We observed that the FOI in the upper part of the cerebral aqueduct was similarly elevated in patients with Hakim’s disease and healthy elderly individuals aged ≥ 60 years. However, we found that the FOI in the third ventricle, particularly in the anterior part, was significantly lower in patients with Hakim’s disease compared to healthy elderly individuals. This difference may be attributed to alterations in CSF dynamics in the third ventricle, where a laminar to vortex flow pattern is established. Furthermore, we found the morphological features of DESH were significantly associated with the FOIs at the cerebral aqueduct and bilateral foramina of Luschka, rather than the foramen of Magendie. In our previous studies [6], we concluded that the enlargement of the foramen of Magendie with aging results in the transmission of CSF pulses into the ventricles, leading to ventricular enlargement. However, we have now discovered that fluid oscillations at the bilateral

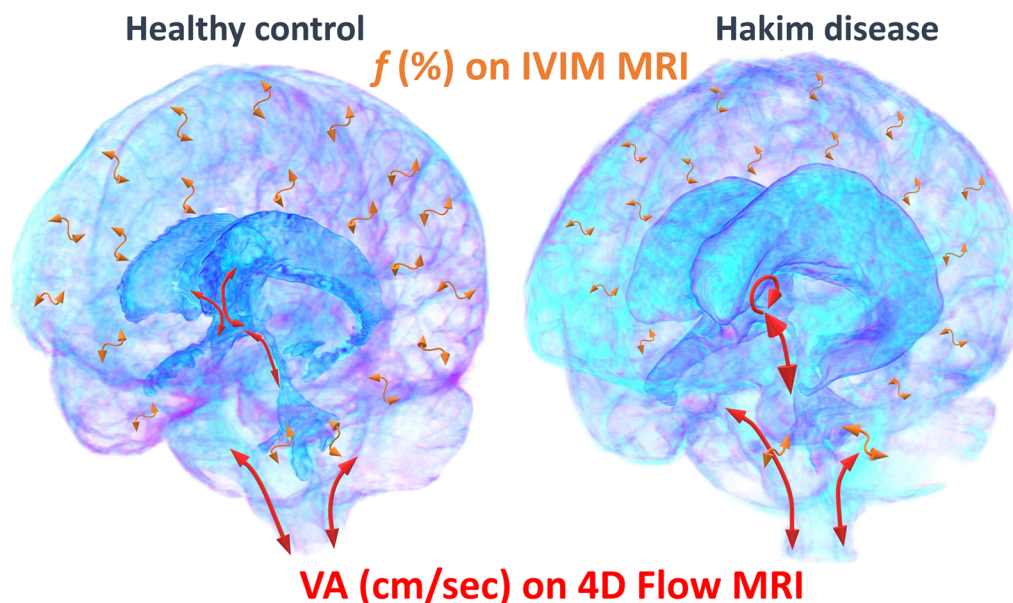


Fig. 7 Illustration of CSF movement in a healthy control and a patient with Hakim’s disease. Compared to healthy controls, patients with Hakim’s disease have larger CSF repetitive movements measured by velocity amplitude (VA) on 4D Flow MRI at the cerebral aqueduct and vortex flow in the third ventricle (red arrows) and smaller CSF repetitive movements measured by *f* on IVIM MRI in the superficial subarachnoid space (orange arrows)

foramina of Luschka may be more closely associated with DESH formation, including ventricular enlargement, compared to those at the foramen of Magendie. CSF movements through the foramen magnum, which is the epicenter of CSF movements, play a dual role: to decrease pressure fluctuations associated with changes in the volume of blood inflow and outflow in the intracranial space during cerebral circulation and to regulate intracranial pressure during positional changes between supine and upright postures [19, 43]. This role requires an extensive spinal subarachnoid space contiguous to the lumbar region, where the CSF moves in and out of the skull base through the foramen magnum. Pulsatile CSF movements require energy according to the law of conservation of energy, and energy consumption can be minimized as much as possible by collecting the CSF near the epicenter, which is the foramen magnum. As CSF increases, it may accumulate close to the foramen magnum, where it is most mobile. Conversely, the supratentorial convexity region located farthest from the foramen magnum, where the CSF is least mobile, may become compressed, resulting in the characteristic morphology of DESH.

We observed an increase in pulsatile CSF motions in the Sylvian fossa, carotid cistern, and ambient cisterns, which contain the major intracranial arteries around the circle of Willis, with aging. However, there was a notable decrease in CSF oscillations in Hakim's disease. Arterial pulsatility tends to increase with age due to aortic stiffness [44–48], but CSF oscillations due to arterial pulsation may be attenuated in Hakim's disease with enlargement of the Sylvian fissure and basal cistern. Aging and various diseases such as hypertension and diabetes have been reported as risk factors for Hakim's disease [8, 49–51], which is known to be caused by arteriosclerosis affecting the dilation and contraction of cerebral arteries [44]. Furthermore, patients with Hakim's disease exhibit shorter and fewer perivascular spaces as well as severe periventricular hyperintensity on MRI compared to healthy controls [52]. Additionally, these abnormal features have been observed to improve after CSF shunt surgery [52]. These findings may be related to dysfunction of the glymphatic system [17, 18] in Hakim's disease. However, the relationship between CSF flow and arterial wall pulsation has not been fully elucidated.

This study has some limitations. First, the distributions of sex and age in the healthy controls aged ≥ 60 years did not match those in the Hakim group. The mean age of the Hakim group was significantly higher than that of healthy controls aged ≥ 60 years. A sufficient number of older controls could have more clearly shown the difference in f -values between brains with Hakim's disease and healthy aging brains. Second, the ROIs on 4D flow MRI and

IVIM MRI were manually placed by a single researcher based on anatomical features; therefore, reproducibility was not ensured. We would like to enable automatic ROI placement in the application. Third, the correlation between the flow velocity parameters on 4D flow MRI and the mean f -values on IVIM MRI was not very strong. Additionally, $VA = 0.4$ cm/s was assumed to correspond to $f = 75\%$ in this study; however, these values may be influenced by sequence parameters such as the $venc$ setting for 4D Flow MRI and the b -values setting for IVIM MRI. Finally, we applied a nonlinear exponential curve regression equation to estimate VA from the mean f -values on IVIM MRI. In the future, age-related changes in CSF dynamics in the entire intracranial CSF space should be simulated using advanced computational fluid dynamics data assimilation of flow velocity data obtained using 4D flow MRI and IVIM MRI to elucidate the mechanism of disproportionate CSF distribution, including DESH, in Hakim's disease. Data assimilation using computational fluid dynamics and lattice models is most effective in situations where complex fluid motions must be predicted.

Conclusions

We comprehensively investigated the CSF dynamics in healthy individuals with ages ranging from their 20 s to 80 s and patients with Hakim's disease (iNPH) by integrating 4D flow MRI and IVIM MRI. We estimated the fluid oscillations in the entire intracranial CSF space using a novel index, the FOI, which combined VA derived from 4D flow MRI with f -values derived from IVIM MRI. In addition, we found the ventricle volume ratio and morphological features of Hakim's disease were significantly associated with the FOIs at the cerebral aqueduct and bilateral foramina of Luschka, rather than the foramen of Magendie. Furthermore, FOIs at the cerebral aqueduct and bilateral foramina of Luschka were elevated in both Hakim's disease and healthy controls aged ≥ 60 years. The computational simulation by estimating CSF motion across the entire intracranial CSF space on both 4D flow MRI and IVIM MRI could help explore the underlying mechanisms of disproportionate expansion of the ventricles and subarachnoid spaces in Hakim's disease.

Abbreviations

| | |
|------|--|
| BVR | Brain per ventricle ratio |
| CSF | Cerebrospinal fluid |
| DESH | Disproportionately enlarged subarachnoid space hydrocephalus |
| DWI | Diffusion weighted image |
| f | Fraction of incoherent perfusion |
| FOI | Fluid oscillation index |
| IVIM | Intravoxel incoherent motion |
| PC | Phase-contrast |
| ROI | Region of interest |
| SD | Standard deviation |
| VA | Velocity amplitude |

Supplementary Information

The online version contains supplementary material available at <https://doi.org/10.1186/s12987-024-00552-6>.

Supplementary Material 1.

Acknowledgements

We thank the radiology staff of Shiga University of Medical Science and Nagoya City University Hospital. We thank Enago (www.enago.jp) for the English language review. We are grateful to FUJIFILM Corporation for allowing us to use the pre-released version of the SYNAPSE 3D workstation.

Author contributions

Shigeki Yamada: conceptualization, methodology, data curation, formal analysis, investigation, resources, project administration, writing—original draft, and visualization. Tomohito Otani: resources, project administration, and supervision. Satoshi Ii: resources, project administration, and supervision. Hiro-taka Ito: developer of applications for analysis, methodology, and supervision. Chifumi Iseki: supervision. Motoki Tanikawa: supervision. yoshiyuki watanabe: resources, project administration, and supervision. Shigeo Wada: resources, project administration, and supervision. Marie Oshima: resources, project administration, and supervision. Mitsuhiro Mase: supervision.

Funding

Shigeki Yamada has received research grants from the Japan Society for the Promotion of Science (JSPS) Grant-in-Aid for Scientific Research (C) for 3 years, beginning in 2021 (Grant No. 21K09098); JSPS Grant-in-Aid for Scientific Research (A) for 4 years, beginning in 2022 (Grant No. 22H00190); JSPS Grant-in-Aid for Scientific Research (B) for 3 years, beginning in 2022 (Grant no. 22H03020); JSPS Grant-in-Aid for Scientific Research (B) for 4 years, beginning in 2024 (Grant No. 24K02557); from the Ministry of Education, Culture, Sports, Science and Technology as “Program for Promoting Researches on the Supercomputer Fugaku” for 4 years, beginning in 2023 (Grant No. DJPMXP1020230118); FUJIFILM Corporation for 4 years, beginning in 2019; G-7 Scholarship Foundation for 1 year in 2020, Osaka Gas Group Welfare Foundation for 1 year in 2022, Taiju Life Social Welfare Foundation for 1 year in 2020, and for 1 year in 2022. The funding sources for the study played no role in the design and conduct of the study, in the collection, analysis, and interpretation of the data, or in the preparation, review, or approval of the manuscript.

Availability of data and materials

The data, including clinical information, collected and analyzed in this study will only be available if the Ethics Committees approve new participation in the collaborative research.

Declarations

Ethics approval and consent to participate

The study design and protocol of this prospective and observational study were approved by the Ethics Committees for Human Research of our institutions (IRB Number: 60-22-0083 and R2019-227). Healthy volunteers underwent MRI after providing written informed consent, and we particularly explained the potential for detecting diseases in the brain. The patients' MRI data were obtained using an opt-out method. All MRI data were extracted after the personal information of the study subjects was anonymized in a linkable manner. The study design was prospective and observational. This study was conducted according to the approved guidelines of the Declaration of Helsinki.

Consent for publication

Not applicable.

Competing interests

Some authors of this manuscript declare their relationship with FUJIFILM Corporation because this study used a SYNAPSE 3D workstation (FUJIFILM Corporation; Tokyo, Japan), as a medical device approved by the Pharmaceuticals and Medical Devices Agency of Japan in 2020. Shigeki Yamada has received research grants from the FUJIFILM Corporation and speakers' honoraria from FUJIFILM Medical Systems since 2019. Hiro-taka Ito is employed by the FUJIFILM

Corporation and has made substantial contributions to the development of the applications of the SYNAPSE 3D workstation. The other authors of this manuscript declare that they have no relationships with any companies whose products or services may be related to the subject matter of the article.

Author details

¹Department of Neurosurgery, Nagoya City University Graduate School of Medical Science, Kawasumi 1, Mizuho-Cho, Mizuho-Ku, Nagoya, Aichi 467-8601, Japan. ²Interfaculty Initiative in Information Studies/Institute of Industrial Science, The University of Tokyo, Tokyo, Japan. ³Department of Mechanical Science and Bioengineering, Graduate School of Engineering Science, Osaka University, Osaka, Japan. ⁴Department of Mechanical Engineering, School of Engineering, Tokyo Institute of Technology, Tokyo, Japan. ⁵Faculty of System Design, Tokyo Metropolitan University, Tokyo, Japan. ⁶Medical System Research & Development Center, FUJIFILM Corporation, Tokyo, Japan. ⁷Department of Behavioural Neurology and Cognitive Neuroscience, Tohoku University Graduate School of Medicine, Sendai, Miyagi, Japan. ⁸Division of Neurology and Clinical Neuroscience, Department of Internal Medicine III, Yamagata University School of Medicine, Yamagata, Japan. ⁹Department of Radiology, Shiga University of Medical Science, Shiga, Japan.

Received: 17 December 2023 Accepted: 21 May 2024

Published online: 30 May 2024

References

- Ohata S, Nakatani J, Herranz-Perez V, Cheng J, Belinson H, Inubushi T, et al. Loss of Dishevelleds disrupts planar polarity in ependymal motile cilia and results in hydrocephalus. *Neuron*. 2014;83(3):558–71.
- Olstad EW, Ringers C, Hansen JN, Wens A, Brandt C, Wachten D, et al. Ciliary beating compartmentalizes cerebrospinal fluid flow in the brain and regulates ventricular development. *Curr Biol*. 2019;29(2):229–241.e6.
- Bradley WG, Queralt SD. Normal-pressure hydrocephalus: evaluation with cerebrospinal fluid flow measurements at MR imaging. *Radiology*. 1996;198:523–9.
- Bradley WG. CSF flow in the brain in the context of normal pressure hydrocephalus. *Am J Neuroradiol*. 2015;36(5):831–8.
- Kahlon B, Annertz M, Stahlberg F, Rehnrcrona S. Is aqueductal stroke volume, measured with cine phase-contrast magnetic resonance imaging scans useful in predicting outcome of shunt surgery in suspected normal pressure hydrocephalus? *Neurosurgery*. 2007;60(1):124–9 (**discussion 9–30**).
- Yamada S, Ishikawa M, Ito H, Yamamoto K, Yamaguchi M, Oshima M, et al. Cerebrospinal fluid dynamics in idiopathic normal pressure hydrocephalus on four-dimensional flow imaging. *Eur Radiol*. 2020;30(8):4454–65.
- Yamada S, Ito H, Ishikawa M, Yamamoto K, Yamaguchi M, Oshima M, et al. Quantification of oscillatory shear stress from reciprocating CSF motion on 4D flow imaging. *Am J Neuroradiol*. 2021;42(3):479–86.
- Yamada S, Ishikawa M, Nozaki K. Exploring mechanisms of ventricular enlargement in idiopathic normal pressure hydrocephalus: a role of cerebrospinal fluid dynamics and motile cilia. *Fluids Barriers CNS*. 2021;18(1):20.
- Chen L, Beckett A, Verma A, Feinberg DA. Dynamics of respiratory and cardiac CSF motion revealed with real-time simultaneous multi-slice EPI velocity phase contrast imaging. *Neuroimage*. 2015;122:281–7.
- Lagana MM, Di Tella S, Ferrari F, Pelizzari L, Cazzoli M, Alperin N, et al. Blood and cerebrospinal fluid flow oscillations measured with real-time phase-contrast MRI: breathing mode matters. *Fluids Barriers CNS*. 2022;19(1):100.
- Yamada S, Miyazaki M, Kanazawa H, Higashi M, Morohoshi Y, Bluml S, et al. Visualization of cerebrospinal fluid movement with spin labeling at MR imaging: preliminary results in normal and pathophysiological conditions. *Radiology*. 2008;249(2):644–52.
- Uribe S, Beerbaum P, Sorensen TS, Rasmussen A, Razavi R, Schaeffter T. Four-dimensional (4D) flow of the whole heart and great vessels using real-time respiratory self-gating. *Magn Reson Med*. 2009;62(4):984–92.
- Lindström EK, Ringstad G, Mardal K-A, Eide PK. Cerebrospinal fluid volumetric net flow rate and direction in idiopathic normal pressure hydrocephalus. *NeuroImage Clin*. 2018;20:731–41.

14. Odeen H, Uppman M, Markl M, Spottiswoode BS. Assessing cerebrospinal fluid flow connectivity using 3D gradient echo phase contrast velocity encoded MRI. *Physiol Meas*. 2011;32(4):407–21.
15. Rivera-Rivera LA, Vikner T, Eisenmenger L, Johnson SC, Johnson KM. Four-dimensional flow MRI for quantitative assessment of cerebrospinal fluid dynamics: status and opportunities. *NMR Biomed*. 2023. <https://doi.org/10.1002/nbm.5082>.
16. Takizawa K, Matsumae M, Hayashi N, Hirayama A, Yatsushiro S, Kuroda K. Hyperdynamic CSF motion profiles found in idiopathic normal pressure hydrocephalus and Alzheimer's disease assessed by fluid mechanics derived from magnetic resonance images. *Fluids Barriers CNS*. 2017;14(1):29.
17. Mestre H, Tithof J, Du T, Song W, Peng W, Sweeney AM, et al. Flow of cerebrospinal fluid is driven by arterial pulsations and is reduced in hypertension. *Nat Commun*. 2018;9(1):4878.
18. Nedergaard M, Goldman SA. Glymphatic failure as a final common pathway to dementia. *Science*. 2020;370(6512):50–6.
19. Baledent O, Henry-Feugeas MC, Idy-Peretti I. Cerebrospinal fluid dynamics and relation with blood flow: a magnetic resonance study with semiautomated cerebrospinal fluid segmentation. *Invest Radiol*. 2001;36(7):368–77.
20. Yamada S, Ito H, Tanikawa M, Ii S, Otani T, Wada S, et al. Age-related changes in cerebrospinal fluid dynamics in the pathogenesis of chronic hydrocephalus in adults. *World Neurosurg*. 2023;178:351–8.
21. Iloff JJ, Wang M, Liao Y, Plogg BA, Peng W, Gundersen GA, et al. A paravascular pathway facilitates CSF flow through the brain parenchyma and the clearance of interstitial solutes, including amyloid beta. *Sci Transl Med*. 2012;4(147):147ra11.
22. Nedergaard M. Neuroscience. Garbage truck of the brain. *Science*. 2013;340(6140):1529–30.
23. Xie L, Kang H, Xu Q, Chen MJ, Liao Y, Thiyagarajan M, et al. Sleep drives metabolite clearance from the adult brain. *Science*. 2013;342(6156):373–7.
24. Kockum K, Lilja-Lund O, Larsson EM, Rosell M, Soderstrom L, Virhammar J, et al. The idiopathic normal-pressure hydrocephalus Radscale: a radiological scale for structured evaluation. *Eur J Neurol*. 2018;25(3):569–76.
25. Sasaki M, Honda S, Yuasa T, Iwamura A, Shibata E, Ohba H. Narrow CSF space at high convexity and high midline areas in idiopathic normal pressure hydrocephalus detected by axial and coronal MRI. *Neuroradiology*. 2008;50(2):117–22.
26. Yamada S, Ito H, Matsumasa H, Tanikawa M, Ii S, Otani T, et al. Tightened sulci in the high convexities as a noteworthy feature of idiopathic normal pressure hydrocephalus. *World Neurosurg*. 2023;176:e427–37.
27. Tullberg M, Toma AK, Yamada S, Laurell K, Miyajima M, Watkins LD, et al. Classification of chronic hydrocephalus in adults: a systematic review and analysis. *World Neurosurg*. 2024;183:113–22.
28. Yamada S, Hiratsuka S, Otani T, Ii S, Wada S, Oshima M, et al. Usefulness of intravoxel incoherent motion MRI for visualizing slow cerebrospinal fluid motion. *Fluids Barriers CNS*. 2023;20(1):16.
29. Le Bihan D, Breton E, Lallemand D, Grenier P, Cabanis E, Laval-Jeantet M. MR imaging of intravoxel incoherent motions: application to diffusion and perfusion in neurologic disorders. *Radiology*. 1986;161(2):401–7.
30. Le Bihan D, Breton E, Lallemand D, Aubin ML, Vignaud J, Laval-Jeantet M. Separation of diffusion and perfusion in intravoxel incoherent motion MR imaging. *Radiology*. 1988;168(2):497–505.
31. Le Bihan D. What can we see with IVIM MRI? *Neuroimage*. 2019;187:56–67.
32. Hashimoto M, Ishikawa M, Mori E, Kuwana N. Diagnosis of idiopathic normal pressure hydrocephalus is supported by MRI-based scheme: a prospective cohort study. *Cerebrospinal Fluid Res*. 2010;7(1):1–11.
33. Yamada S, Ishikawa M, Yamamoto K. Optimal diagnostic indices for idiopathic normal pressure hydrocephalus based on the 3D quantitative volumetric analysis for the cerebral ventricle and subarachnoid space. *Am J Neuroradiol*. 2015;36(12):2262–9.
34. Yamada S, Ishikawa M, Yamamoto K. Comparison of CSF distribution between idiopathic normal pressure hydrocephalus and Alzheimer disease. *Am J Neuroradiol*. 2016;37(7):1249–55.
35. Nakajima M, Yamada S, Miyajima M, Ishii K, Kuriyama N, Kazui H, et al. Guidelines for management of idiopathic normal pressure hydrocephalus (third edition): endorsed by the Japanese society of normal pressure hydrocephalus. *Neurol Med Chir*. 2021;52(11):775–809.
36. Yavuz Ilik S, Otani T, Yamada S, Watanabe Y, Wada S. A subject-specific assessment of measurement errors and their correction in cerebrospinal fluid velocity maps using 4D flow MRI. *Magn Reson Med*. 2022;87(5):2412–23.
37. Yamada S, Ishikawa M, Iwamuro Y, Yamamoto K. Choroidal fissure acts as an overflow device in cerebrospinal fluid drainage: morphological comparison between idiopathic and secondary normal-pressure hydrocephalus. *Sci Rep*. 2016;6:39070.
38. Ishii K, Kanda T, Harada A, Miyamoto N, Kawaguchi T, Shimada K, et al. Clinical impact of the callosal angle in the diagnosis of idiopathic normal pressure hydrocephalus. *Eur Radiol*. 2008;18(11):2678–83.
39. Yamada S, Mase M. Cerebrospinal fluid production and absorption and ventricular enlargement mechanisms in hydrocephalus. *Neurol Med Chir*. 2023;63(4):141–51.
40. Yamada S, Otani T, Ii S, Kawano H, Nozaki K, Wada S, et al. Aging-related volume changes in the brain and cerebrospinal fluid using artificial intelligence-automated segmentation. *Eur Radiol*. 2023;33(10):7099–112.
41. Bethlehem RAI, Seidlitz J, White SR, Vogel JW, Anderson KM, Adamson C, et al. Brain charts for the human lifespan. *Nature*. 2022;604(7906):525–33.
42. Leenders KL, Perani D, Lammertsma AA, Heather JD, Buckingham P, Healy MJ, et al. Cerebral blood flow, blood volume and oxygen utilization. Normal values and effect of age. *Brain*. 1990;113(Pt 1):27–47.
43. Owashi KP, Capel C, Baledent O. Cerebral arterial flow dynamics during systole and diastole phases in young and older healthy adults. *Fluids Barriers CNS*. 2023;20(1):65.
44. Fonck E, Feigl GG, Fasel J, Sage D, Unser M, Rufenacht DA, et al. Effect of aging on elastin functionality in human cerebral arteries. *Stroke*. 2009;40(7):2552–6.
45. Lefferts WK, DeBlois JP, Augustine JA, Keller AP, Heffernan KS. Age, sex, and the vascular contributors to cerebral pulsatility and pulsatile damping. *J Appl Physiol*. 2020;129(5):1092–101.
46. Smulyan H, Mookherjee S, Safar ME. The two faces of hypertension: role of aortic stiffness. *J Am Soc Hypertens*. 2016;10(2):175–83.
47. Tarumi T, Ayaz Khan M, Liu J, Tseng BY, Parker R, Riley J, et al. Cerebral hemodynamics in normal aging: central artery stiffness, wave reflection, and pressure pulsatility. *J Cereb Blood Flow Metab*. 2014;34(6):971–8.
48. Zarrinkoob L, Ambarki K, Wahlin A, Birgander R, Carlberg B, Eklund A, et al. Aging alters the dampening of pulsatile blood flow in cerebral arteries. *J Cereb Blood Flow Metab*. 2016;36(9):1519–27.
49. Hudson M, Nowak C, Garling RJ, Harris C. Comorbidity of diabetes mellitus in idiopathic normal pressure hydrocephalus: a systematic literature review. *Fluids Barriers CNS*. 2019;16(1):5.
50. Jaraj D, Agerskov S, Rabiei K, Marlow T, Jensen C, Guo X, et al. Vascular factors in suspected normal pressure hydrocephalus: a population-based study. *Neurology*. 2016;86(7):592–9.
51. Rasanen J, Huovinen J, Korhonen VE, Junkkari A, Kastinen S, Komulainen S, et al. Diabetes is associated with familial idiopathic normal pressure hydrocephalus: a case–control comparison with family members. *Fluids Barriers CNS*. 2020;17(1):57.
52. Ishikawa M, Yamada S, Yamamoto K. Three-dimensional observation of Virchow-Robin spaces in the basal ganglia and white matter and their relevance to idiopathic normal pressure hydrocephalus. *Fluids Barriers CNS*. 2015;12:15.

Publisher's Note

Springer Nature remains neutral with regard to jurisdictional claims in published maps and institutional affiliations.

Shigeki Yamada serve as board members of the International Society for Hydrocephalus and Cerebrospinal Fluid Disorders (ISHCSF).

Mitsuhiro Mase serve as board members of the International Society for Hydrocephalus and Cerebrospinal Fluid Disorders (ISHCSF). M.M. will be responsible for organizing the 16th Hydrocephalus Meeting 2024 in Nagoya, Japan.